
Growing a Neural Network in Breadth, Depth, and Time

Eivinas Butkus^{1,2} Kedar Garzón Gupta¹ Nikolaus Kriegeskorte^{1,2}
eb3407@columbia.edu kg3162@columbia.edu nk2765@columbia.edu

¹Columbia University

²NSF AI Institute for Artificial and Natural Intelligence

Abstract

Spatial and temporal resource constraints are critical for both biological and artificial intelligent systems. Here we define differentiable cost terms for breadth, depth, and time within a recurrent convolutional neural network conceived as a finite subset of an infinite lattice. We optimize these costs jointly with task errors via backpropagation. We set different pressures on breadth, depth, and time, which leads to diverse computational graphs emerging organically through training. We find that all three resources can be traded off against each other to achieve a given level of accuracy. Networks grow in all three dimensions with task complexity and spontaneously take more recurrent steps when inputs are occluded. Surprisingly, time used by the model correlates with human reaction times in an object recognition task. Our framework provides a normative account of how resource constraints shape neural architectures, connecting to questions about brain design in neuroscience, and may help illuminate the diversity of neural solutions found in nature.

1 Introduction

Intelligence—both biological and artificial—can be broadly characterized as the capacity to achieve goals under resource constraints [34, 13, 27]. Two important resources for brains and AI systems are *space* and *time*. In brains, each additional neuron adds metabolic costs, maintenance, and wiring—making a smaller brain preferable [8, 21, 38]. A faster brain confers advantages too [39]: failing to quickly detect a predator may lead to death. Thus, to understand a brain fully, we should consider not only the particular problems it solves (such as visual recognition), but also the particular set of spatial and temporal resource constraints it has evolved under. Engineers face analogous pressures, motivating work on model compression [15, 16], knowledge distillation [17], architecture search [29], and adaptive computation [14, 35].

In this work, we consider three resources: breadth, depth, and time. Traditionally, these are treated as fixed hyperparameters, explored via grid search or manual tuning. Prior work has gone further: pruning methods reduce breadth and depth post-hoc [15, 11], network slimming learns channel importance via differentiable sparsity penalties [31], and adaptive computation time optimizes time allocation through backpropagation [14]. However, no prior work has optimized all three *jointly* within a single framework.

Here we define differentiable cost terms for breadth, depth, and time, and optimize those jointly with errors using backpropagation. This setup lets a network *grow* organically in all three dimensions, finding its own trade-off between resources and errors based on the pressures applied. To visualize this process, one can think of an infinite lattice that extends along breadth, depth, and time (Fig. 1). A single computational graph (model instance) is grown in this space, resulting in a unique profile of resource use.

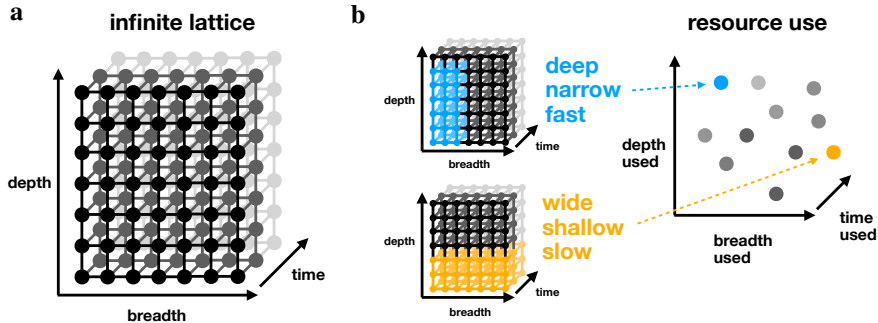


Figure 1: **a** The space of possible computational graphs can be conceptualized as an infinite lattice, extending in the space of resource use. Here we consider breadth, depth, and time. **b** Each model instance is a finite subset of the infinite lattice with its own profile of resource use. Our framework lets the network select its own position in this space by optimizing differentiable resource costs.

We implement the lattice using a recurrent convolutional neural network architecture with bottom-up, lateral, and top-down connections, where breadth corresponds to channels, depth to layers, and time to recurrent processing steps (Fig. 2). Under a given set of resource pressures, the optimization process organically prunes channels, layers, and time steps, carving out a compact subgraph from the full architecture. We train over a thousand models spanning the space of resource pressures.

We find that breadth, depth, and time are fungible: shallow-wide networks can match the accuracy of deep-narrow ones, and all three resources can compensate for one another. Adaptive time allocation emerges organically—models spontaneously take more recurrent steps when inputs are occluded—and the time the model spends on individual images correlates with human reaction times, despite never being trained on human data. Networks grow in all three dimensions with task complexity, using more resources for more complex datasets.

Our main contributions are:

1. A differentiable, modular, and extensible multi-resource cost (MRC) framework that jointly optimizes breadth, depth, and time costs alongside task errors via backpropagation.
2. The first joint exploration of trade-offs between breadth, depth, and time, showing that all three resources are fungible.
3. The finding that adaptive time allocation emerges organically and correlates with human reaction times, linking computational resource optimization to human perception.

Our framework enables efficient exploration of the space of possible architectures, and may help illuminate the diversity of neural solutions found in nature.

2 Related work

The idea that intelligent systems operate under resource constraints has a long history. Simon’s bounded rationality [34] proposed that decision-makers optimize within cognitive limits, an idea formalized more recently as computational rationality [13] and resource rationality [27]. Symbolic and probabilistic computational models have explored how resource-rational agents perceive and make decisions [40, 18, 3]. These works study resource constraints at the cognitive level. We impose them at the level of neural architecture (on the wiring and dynamics of the network itself).

In computational neuroscience, spatial resource constraints have been studied through the lens of wiring economy—the principle that neural circuits minimize wiring costs [8, 6, 1]. Recent work has imposed spatial constraints on neural network models to better account for the topographic organization of visual cortex [28, 4, 32]. On the temporal side, recurrent neural networks have been used to study the role of recurrent processing in biological vision, showing that recurrence helps explain the dynamics of human object recognition [36, 19, 37]. Our work extends this line of research by jointly considering spatial and temporal resource costs within a single framework.

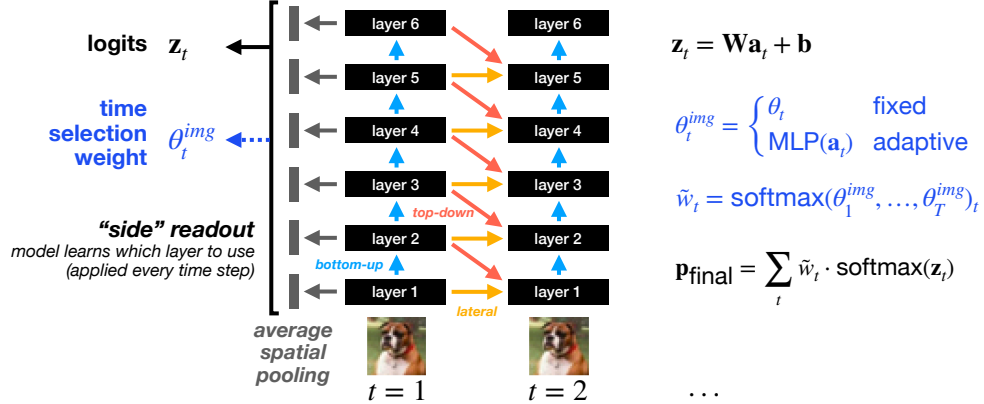


Figure 2: **Model architecture.** The network implements a finite subset of the infinite lattice (Fig. 1), within which computational graphs of different effective breadth (channels used), depth (layers used), and time (recurrent time steps used) emerge through training. It is a recurrent convolutional network with bottom-up (feedforward), lateral (recurrent within-layer), and top-down (feedback) connections. At each time step, every layer receives input from all three connection types, and maintains a hidden state that accumulates information over time. A side readout applied at every time step allows the model to read from any layer—the network learns which layers are useful rather than being forced to use the deepest one. Time selection weights determine how much the final prediction relies on each time step: these can be fixed (shared across all inputs) or adaptive (input-dependent via a small MLP). Under resource pressure, the network organically prunes channels, layers, and time steps it does not need, carving out a compact subgraph from the full architecture.

In deep learning, prior work has trained models with adaptive depth [7], breadth [31], and time [14] through backpropagation. Pruning methods reduce network size post-hoc by removing units that contribute least to performance [24, 15, 26, 11], though effective pruning typically requires iterative cycles of removal and fine-tuning. Neural architecture search methods explore the space of possible architectures [29], including differentiable approaches that optimize architecture parameters via gradient descent [30]. However, these methods search over discrete architectural choices (e.g., which operations to use), rather than imposing continuous resource costs on a fixed computational graph. Our work is the first to jointly optimize differentiable costs for breadth, depth, and time within a single framework.

3 Methods

3.1 Multi-resource cost (MRC) optimization

A typical loss for a neural network includes only task performance (e.g., cross-entropy) and regularization (e.g., weight decay). Our approach adds differentiable cost terms for multiple resources and studies the trade-offs that emerge between them. We consider four terms in the loss:

$$\mathcal{L} = \underbrace{\lambda_{\text{errors}} \mathcal{L}_{\text{errors}}}_{\text{errors}} + \underbrace{\lambda_{\text{breadth}} \mathcal{L}_{\text{breadth}} + \lambda_{\text{depth}} \mathcal{L}_{\text{depth}}}_{\text{space}} + \underbrace{\lambda_{\text{time}} \mathcal{L}_{\text{time}}}_{\text{time}} \quad (1)$$

The λ coefficients control the relative price of each resource: higher λ values pressure the network to use less of that resource. We fix $\lambda_{\text{errors}} = 1$ throughout and vary only the price of breadth, depth, and time. The framework is readily extensible—one can add further terms (e.g., energy expenditure [5, 2]) and study the resulting trade-offs.

3.2 Model

One can think of the model as implementing the infinite lattice in breadth, depth, and time (Fig. 1). Each model instance is then a finite subset of this lattice, trained under a different set of pressures. In practice, the lattice is implemented by a finite computational graph (Fig. 2).

Input. All images are resized to $32 \times 32 \times 3$ and passed through an initial convolution to map the input channels to $C = 48$ feature channels.

Recurrent convolutional network. The model is a recurrent convolutional network with $L = 6$ layers and $T = 5$ time steps. At each time step t , each layer i receives three inputs combined additively: a bottom-up signal from layer $i-1$ at the current time step, a lateral signal from layer i at the previous time step, and a top-down signal from layer $i+1$ at the previous time step (Fig. 2). The top layer receives no top-down input. All connections are 3×3 convolutions with $C = 48$ output channels. Each layer maintains a hidden state $\mathbf{h}_{t,i}$ that accumulates input across time steps, followed by a ReLU nonlinearity. Divisive normalization is applied to both the bottom-up input and the lateral and top-down signals. We add Gaussian noise ($\sigma = 0.1$) to the hidden states at each time step (see motivation in Appendix C).

Side readout. At each time step t , the post-ReLU hidden states are spatially average-pooled and concatenated across layers, yielding $\mathbf{a}_t \in \mathbb{R}^{L \cdot C}$. A linear layer maps this to class logits: $\mathbf{z}_t = \mathbf{W}\mathbf{a}_t + \mathbf{b}$.

Time selection. The model produces class logits at every time step, but must select how much to rely on each time step. We consider two variants: *Fixed* time selection uses learnable parameters $\theta_1, \dots, \theta_T$ shared across all inputs—the model learns a single temporal allocation applied uniformly. *Adaptive* time selection computes a scalar weight at each time step as a function of the current pooled image-dependent activations via a small two-layer MLP: $\theta_t^{\text{img}} = \text{MLP}(\mathbf{a}_t)$. This allows the model to allocate different amounts of processing time to different inputs. In both cases, the raw time selection weights are ℓ_2 -normalized, scaled by a fixed temperature ($\tau = 4$), and passed through a softmax to obtain the time selection weights $\tilde{w}_1, \dots, \tilde{w}_T$ ($\tilde{w}_i \in [0.017, 0.932]$, ensuring gradients flow to all time steps during training).

Output. The final output is a mixture of per-timestep probability distributions, weighted by the time selection weights: $\mathbf{p}_{\text{final}} = \sum_t \tilde{w}_t \cdot \text{softmax}(\mathbf{z}_t)$.

3.3 Costs

Errors. The error cost is the cross-entropy between model predictions and dataset labels, normalized by $\log K$ where K is the number of classes:

$$\mathcal{L}_{\text{errors}} = -\frac{1}{\log K} \frac{1}{N} \sum_{n=1}^N \log p_{n,y_n} \quad (2)$$

where p_{n,y_n} is the predicted probability for the correct class of sample n . This normalization ensures the error cost is comparable across datasets with different numbers of classes (e.g., $K = 10$ for CIFAR-10 vs. $K = 200$ for Tiny ImageNet), with a value of 1.0 corresponding to chance-level performance.

Breadth. Within each layer, output channels are sorted by their average weight magnitude across all convolutional kernels (bottom-up, lateral, and top-down). The breadth cost applies a weight decay that scales with channel rank:

$$\mathcal{L}_{\text{breadth}} = \frac{1}{LC} \sum_{i=1}^L \sum_{k=1}^C \left(\frac{k}{C}\right)^\gamma \bar{w}_{i,\pi_i(k)} \quad (3)$$

where $\bar{w}_{i,\pi_i(k)}$ is the mean absolute weight of the channel with rank k in layer i , π_i is the permutation that sorts channels by descending magnitude, and γ is a position power controlling the steepness of the penalty ($\gamma = 4$, chosen to produce a sharp cutoff between used and unused channels). The rank-dependent scaling allows the network to organically consolidate useful features into a few high-magnitude channels while pushing unused channels toward zero.

Depth. The depth cost applies a weight decay that scales with layer index:

$$\mathcal{L}_{\text{depth}} = \frac{1}{LC} \sum_{i=1}^L \left(\frac{i}{L}\right)^\gamma \sum_{k=1}^C \bar{w}_{i,k} \quad (4)$$

Deeper layers are penalized more heavily, pressuring the network to solve the task with fewer layers when possible. The same position power $\gamma = 4$ is applied as for the breadth cost.

Time. The time cost is the expected normalized time step under the time selection weights:

$$\mathcal{L}_{\text{time}} = \sum_{t=1}^T \tilde{w}_t \cdot \frac{t}{T-1} \quad (5)$$

where \tilde{w}_t are the time selection weights. For *fixed* time selection, this cost is the same for all inputs. For *adaptive* time selection, the cost varies per input—the network learns to spend more time on images where the reduction in error cost outweighs the additional time cost.

Optimization. Resource costs and noise are both annealed during training to ensure stable learning (Appendix D). All models are trained for 150 epochs using AdamW with cosine learning rate decay (Appendix E). Each experimental condition is trained across multiple independent instances with different random seeds (Appendix B).

3.4 Definitions of resources used

To quantify the effective resources used by each trained model, we apply a post-hoc pruning procedure that identifies the smallest sub-network preserving 98% of above-chance accuracy (details in Appendix F). The result is a binary mask over layers and channels, from which we define:

Layers used (depth): the number of layers with at least one surviving channel.

Channels used (breadth): the average number of surviving channels per active layer.

Time used: the expected time step index under the time selection weights, $\sum_t \tilde{w}_t \cdot t$.

3.5 Experiments

We use CIFAR-10 [20] as our main dataset across all experiments. Full experimental configurations are provided in Appendix B.

Breadth vs. depth. We vary λ_{breadth} and λ_{depth} across six orders of magnitude each ($\{0, 1, 10, 10^2, 10^3, 10^4\}$) with $\lambda_{\text{time}} = 0$, yielding a 6×6 grid of resource pressure combinations.

Time. We vary λ_{time} from 0 to 1 in increments of 0.1, comparing fixed and adaptive time selection schemes with no space costs ($\lambda_{\text{breadth}} = \lambda_{\text{depth}} = 0$). This is the only experiment using fixed time selection—all other experiments use the adaptive scheme.

Breadth vs. depth vs. time. We vary all three cost factors jointly, combining the breadth and depth grid above with six levels of $\lambda_{\text{time}} \in \{0, 0.1, 0.2, 0.3, 0.5, 1.0\}$.

Task complexity. We compare MNIST [25], CIFAR-10, and Tiny ImageNet [23] (a 200-class subset of ImageNet [9]), varying λ_{breadth} , λ_{depth} , and λ_{time} identically across all three datasets to test whether networks grow with task complexity.

Error bars denote 95% confidence intervals across model instances using the t -distribution. Shaded regions in Fig. 4c,g,h denote 95% bootstrap confidence intervals.

4 Results

4.1 Breadth vs. depth

We begin by considering breadth and depth costs alone, setting $\lambda_{\text{time}} = 0$. Raw costs $\mathcal{L}_{\text{breadth}}$ and $\mathcal{L}_{\text{depth}}$ decrease smoothly with increasing λ_{breadth} and λ_{depth} (Fig. 3a), confirming that the differentiable cost terms work as intended.

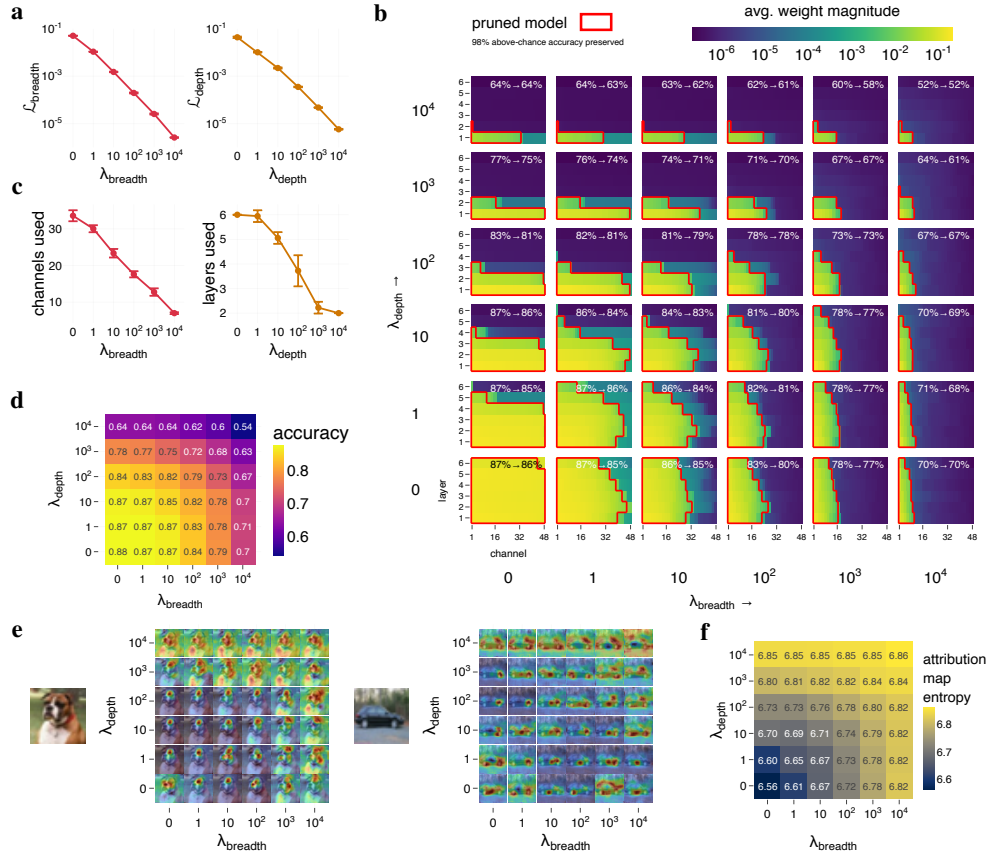


Figure 3: **Breadth vs. depth.** **a** Raw costs decrease smoothly with increasing λ_{breadth} and λ_{depth} . **b** Average weight magnitudes across layers and channels for each λ combination, with pruned model boundaries shown in red (preserving 98% above-chance accuracy). Top right of each panel shows accuracy before \rightarrow after pruning. Shallow-and-wide models (top left) can achieve comparable accuracy to narrow-and-deep models (bottom right). **c** Pruning-defined resources used (channels, layers) decrease as a function of λ . **d** Accuracy decreases with breadth and depth pressure. **e** Attribution maps using input perturbation for two example images (dog and car). Constrained models rely on low-level features spread across the image, while less constrained models attend to high-level features (e.g., the dog’s face). **f** Attribution map entropy (across 100 images and 3 model instances) quantifying attribution map spread as a function of λ_{breadth} and λ_{depth} .

To understand the solutions that emerge, we visualize the average weight magnitude across layers and channels for each λ combination (Fig. 3b). As costs increase, weights concentrate into fewer layers and channels, with the pruning boundary (red outline) shrinking accordingly. Our pruning procedure (Appendix F) recovers compact sub-networks that preserve 98% of above-chance accuracy without fine-tuning, confirming that the resource costs produce genuinely sparse solutions rather than merely scaling down all weights uniformly. The pruning-defined resources—channels used and layers used—decrease as a function of λ (Fig. 3c).

Accuracy decreases with increasing resource pressure (Fig. 3d), but the pattern reveals an important trade-off: shallow-and-wide models (high λ_{depth} , low λ_{breadth}) can achieve comparable accuracy to narrow-and-deep models (low λ_{depth} , high λ_{breadth}). Breadth and depth are thus partially fungible for a given level of performance.

Finally, we ask whether models with different resource profiles rely on different features. We hypothesized that shallow models in particular would rely on low-level features spread throughout the image since they do not have sufficient depth to compose hierarchical higher-level features. Using input perturbation [41], we generate attribution maps showing which image regions drive classification (Fig. 3e). Models heavily constrained in both breadth and depth appear to rely on

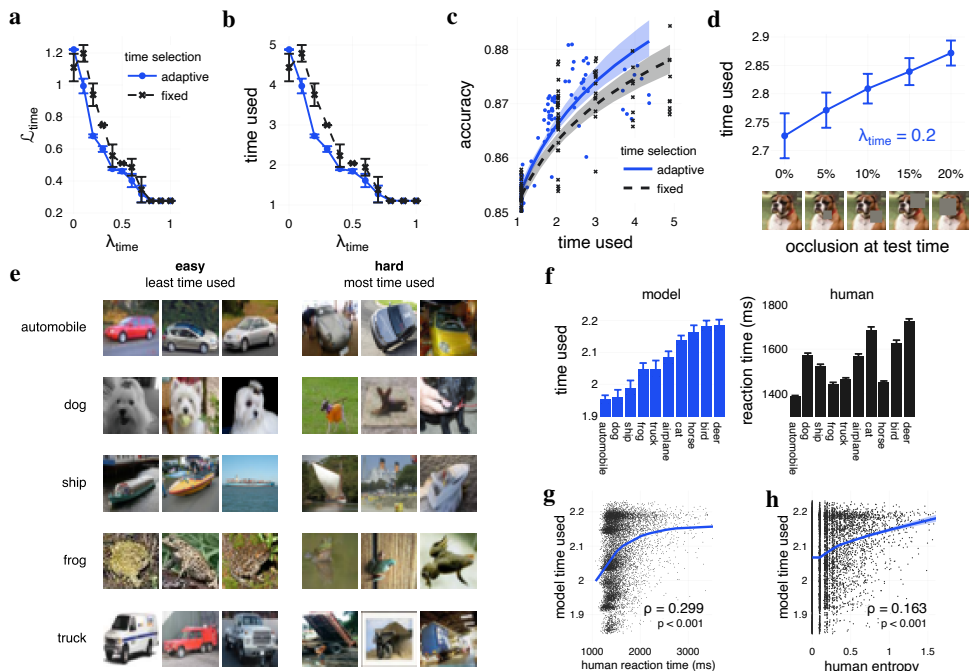


Figure 4: **Time.** **a** λ_{time} vs. time cost $\mathcal{L}_{\text{time}}$. **b** λ_{time} vs. time used. **c** Time used vs. accuracy: adaptive time selection dominates fixed. **d** Occlusion introduced at test time increases time used, demonstrating that the model adaptively chooses how long to compute. **e-h** Adaptive model behavior averaged across all $\lambda_{\text{time}} > 0$. **e** Easy and hard images for several categories, defined by model time used. Model spends more time on ambiguous images. **f** Average model time used and human reaction time per category, sorted by model time used. **g** Image-level correlation between median human reaction times and model time used. **h** Image-level correlation between human judgment uncertainty (entropy across participants) and model time used.

low-level features spread across the image, while less constrained models attend to high-level features such as the dog’s face or the car’s tires. We quantify this using the entropy of the attribution maps (Fig. 3f): more constrained models produce higher-entropy (more diffuse) attribution maps, consistent with a reliance on spatially distributed low-level features. We note that attribution map entropy is strongly correlated with overall accuracy, making it difficult to fully disentangle the effect of depth from performance. At matched accuracy levels, there is a trend toward higher entropy for shallower models, but the effect is small (see Fig. 7 in Appendix H). A more controlled investigation is left for future work.

4.2 Time: adaptive processing emerges

We now turn to time, where we set $\lambda_{\text{breadth}} = \lambda_{\text{depth}} = 0$. Unlike spatial resources, which are fixed properties of the architecture, time can be dynamically adapted at inference—the network can choose to run longer on some inputs than others. This motivates comparing fixed and adaptive time selection: fixed selection treats time like space (same allocation for all inputs), while adaptive selection exploits this asymmetry.

We first confirm that the time cost works as expected: $\mathcal{L}_{\text{time}}$ decreases with increasing λ_{time} (Fig. 4a), and time used decreases accordingly (Fig. 4b). Both fixed and adaptive time selection reduce time used under pressure, but adaptive time selection consistently achieves higher accuracy at every level of time used (Fig. 4c). The ability to allocate time per input dominates fixed allocation.

The adaptive model also exhibits sensible behavior on out-of-distribution inputs. When occlusion is introduced at test time—something the model has never seen during training—time used increases with the proportion of the image occluded (Fig. 4d). The model spontaneously chooses to compute

longer when inputs are degraded. Examining individual images, the model spends the least time on canonical, easy-to-classify examples and the most time on ambiguous or atypical images (Fig. 4e).

Finally, we compare the model’s time allocation to human behavior using the CIFAR-10H dataset [33], which provides per-image human reaction times and classification distributions. At the category level, the ordering of model time used across the ten CIFAR-10 classes qualitatively matches the ordering of human reaction times (Fig. 4f). At the image level, model time used is significantly correlated with human reaction times ($\rho = 0.299, p < 0.001$; Fig. 4g) and with human judgment uncertainty, measured as the entropy of participant responses ($\rho = 0.163, p < 0.001$; Fig. 4h). These correlations emerge despite the model never being trained on human data. The pressure to use time efficiently under a time cost is sufficient to produce human-like adaptive processing behavior.

4.3 Breadth vs. depth vs. time

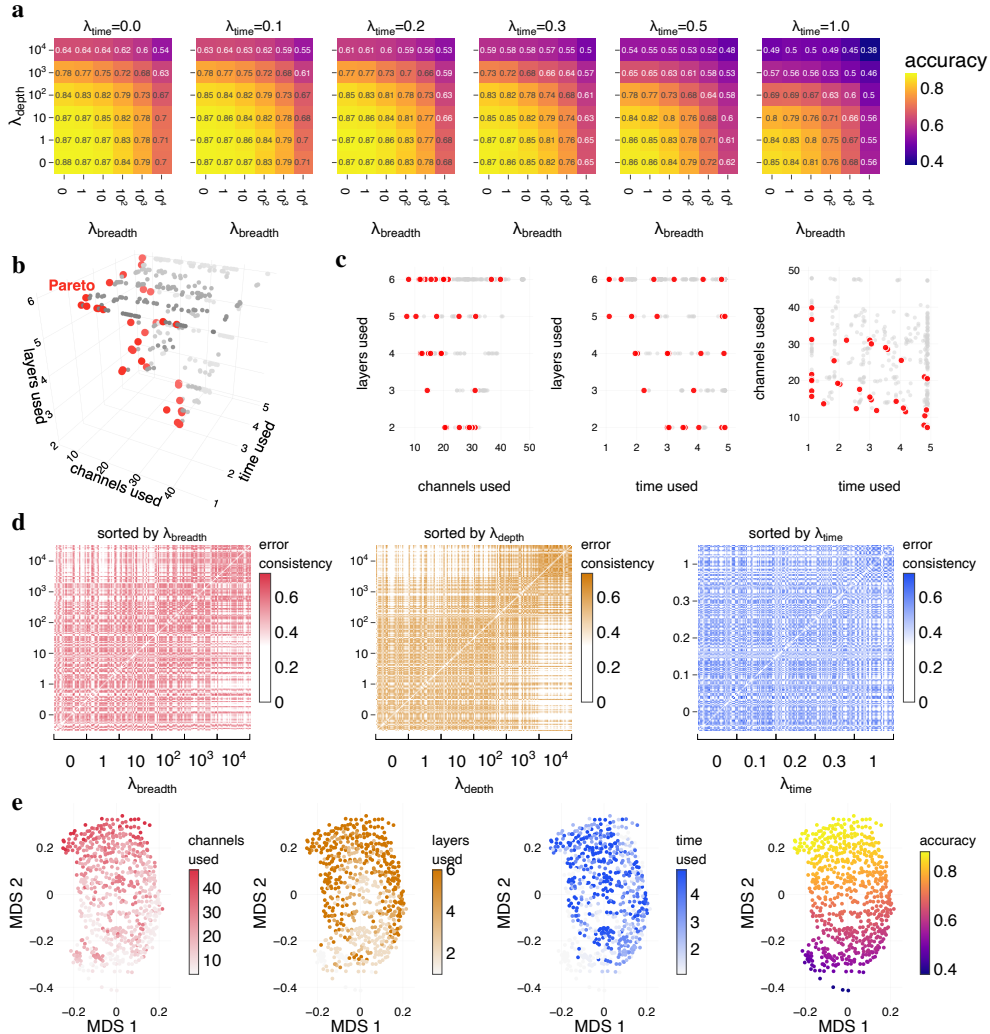


Figure 5: **Breadth vs. depth vs. time.** **a** Accuracy as a function of λ_{breadth} and λ_{depth} for increasing λ_{time} (left to right). **b** Pareto-optimal models (red) that achieve $\geq 70\%$ accuracy while minimizing breadth, depth, and time used, shown in 3D resource space. **c** Pairwise 2D projections of the Pareto set. Red points spread across all projections, indicating that breadth, depth, and time are fungible. **d** Error consistency between model configurations (controlling for chance agreement), sorted by each resource cost. Depth sorting reveals that shallow and deep models make qualitatively different errors. **e** MDS embedding based on pairwise Jensen-Shannon divergence of model output distributions, colored by channels used, layers used, time used, and accuracy.

We now turn to optimizing all three resource costs jointly. Accuracy decreases as any of the three costs increase, but the pattern of degradation depends on the combination (Fig. 5a): increasing λ_{time} compresses the accuracy grid, confirming that time pressure compounds with space pressure.

To understand whether the three resources are interchangeable, we identify the Pareto set of models that achieve at least 70% accuracy while minimizing resource use (Fig. 5b). The Pareto-optimal models (red) span all three resource dimensions, and the 2D projections (Fig. 5c) show that Pareto points spread across each pairwise comparison. This indicates that breadth, depth, and time are fungible: a model can compensate for less of one resource by using more of another. The 70% threshold was chosen to include a sufficient number of models in the Pareto set. The trade-offs are qualitatively similar at higher accuracy thresholds, though the set of feasible solutions naturally narrows.

Beyond accuracy, we ask whether models with different resource profiles arrive at the same solutions. We compute error consistency [12] between all pairs of model configurations, which controls for classifier agreement expected by chance (Fig. 5d). Models sorted by λ_{depth} show a clear block structure: shallow models (Fig. 5d, middle) make a consistent set of mistakes that differs from deep models, suggesting that depth qualitatively changes the solution strategy rather than simply reducing capacity. The breadth sorting shows weaker but still visible structure, while the time sorting shows little clear block structure beyond the diagonal.

Finally, we embed all models in 2D using MDS on pairwise Jensen-Shannon divergence of their output distributions (Fig. 5e). The embeddings reveal that model outputs are structured beyond what accuracy alone captures: channels used, layers used, time used, and accuracy each organize the space along partially distinct axes, confirming that these resources shape behavior in complementary ways.

4.4 Networks grow with task complexity

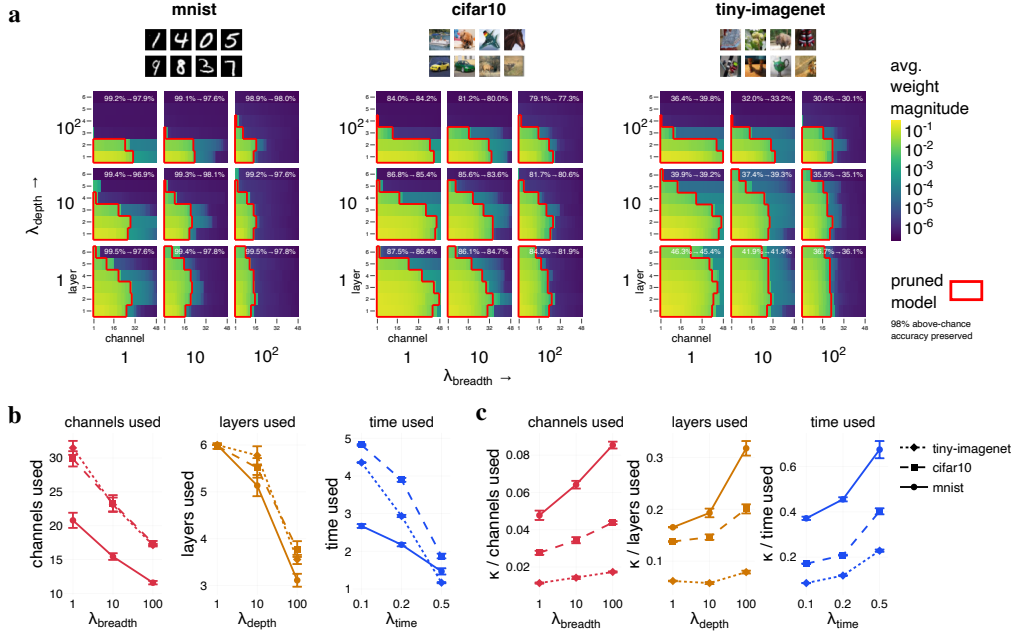


Figure 6: **Task complexity.** **a** Weight magnitude maps across layers and channels for MNIST, CIFAR-10, and Tiny ImageNet under matched resource pressures ($\lambda_{\text{time}} = 0.1$, single model instance shown per panel). Networks grow in breadth and depth as the task becomes more complex. **b** Resources used (channels, layers, time) as a function of resource pressure for each dataset. CIFAR-10 and Tiny ImageNet use more spatial resources than MNIST. **c** Resource efficiency ($\kappa / \text{resource used}$), where $\kappa = (\text{acc} - \text{chance}) / (1 - \text{chance})$. MNIST models are most efficient, extracting the most normalized performance per unit of resource, while Tiny ImageNet models are least efficient.

We test whether networks organically grow in breadth, depth, and time when the task becomes more complex, holding resource pressures fixed. This flips the typical script: the task together with resource pressures (not the engineer) determine the architecture. We compare three datasets of increasing difficulty: MNIST [25], CIFAR-10 [20], and Tiny ImageNet [23] (200 classes). Because our error cost is normalized by $\log K$ (where K is the number of classes), it is comparable across datasets with different numbers of classes.

The weight magnitude maps (Fig. 6a) show that more complex tasks produce denser networks: MNIST models are highly sparse under the same resource pressures that leave CIFAR-10 and Tiny ImageNet models substantially fuller. Quantitatively, CIFAR-10 and Tiny ImageNet models use more channels and layers than MNIST models across all levels of resource pressure (Fig. 6b). Interestingly, Tiny ImageNet models use slightly less time than CIFAR-10 models, possibly because CIFAR-10’s 32×32 images are more ambiguous—consistent with the high levels of human disagreement documented in CIFAR-10H [33] and with our earlier finding that adaptive models spend more time on degraded inputs.

We also measure resource efficiency as $\kappa / \text{resource used}$, where $\kappa = (\text{acc} - \text{chance}) / (1 - \text{chance})$ captures chance-normalized performance (Fig. 6c). MNIST models are the most efficient across all three resources, while Tiny ImageNet models are the least efficient—each unit of resource yields less normalized performance on the harder task. This may partly explain why CIFAR-10 and Tiny ImageNet models use similar amounts of breadth and depth: for Tiny ImageNet, adding more channels or layers does not improve normalized performance as much as it does for other datasets.

5 Discussion

We introduced a multi-resource cost framework that jointly optimizes breadth, depth, and time via backpropagation, and showed that all three resources can be traded off against one another and grow organically with task complexity. Adaptive time allocation emerges naturally under time pressure and correlates with human reaction times, suggesting that resource optimization alone can produce human-like processing dynamics.

Limitations. Our networks are small-to-intermediate in scale. Whether the same trade-offs hold for larger models remains to be tested. The linear combination of costs in the loss may not capture interactions between resources. For instance, in biological systems, speed and accuracy are jointly necessary (detecting a predator slowly is as fatal as not detecting it at all), which suggests a multiplicative or threshold-based combination. We also do not benchmark against existing methods for adaptive depth [7], breadth [31], or time [14] individually, as our goal is to study the joint trade-offs between resources rather than to maximize performance on any single dimension.

Future directions. The MRC framework is readily extensible to additional resource costs such as energy [2, 5] or data efficiency. We plan to use this framework to study the diversity of neural architectures found in nature [22]: different combinations of resource pressures and task demands can be interpreted as defining ecological niches, and the solutions that emerge under each may illuminate why brains are built the way they are.

References

- [1] Jascha Achterberg, Danyal Akarca, D. J. Strouse, John Duncan, and Duncan E. Astle. Spatially embedded recurrent neural networks reveal widespread links between structural and functional neuroscience findings. *Nature Machine Intelligence*, 5(12):1369–1381, November 2023. ISSN 2522-5839. doi: 10.1038/s42256-023-00748-9. URL <https://www.nature.com/articles/s42256-023-00748-9>.
- [2] Abdullahi Ali, Nasir Ahmad, Elgar de Groot, Marcel Antonius Johannes van Gerven, and Tim Christian Kietzmann. Predictive coding is a consequence of energy efficiency in recurrent neural networks. *Patterns*, 3(12), 2022.
- [3] Mario Belledonne, Eivinas Butkus, Brian J Scholl, and Ilker Yildirim. Adaptive computation as a new mechanism of dynamic human attention. *Psychological Review*, 133(3):534, 2026.
- [4] Nicholas M Blauch, Marlene Behrmann, and David C Plaut. A connectivity-constrained computational account of topographic organization in primate high-level visual cortex. *Proceedings of the National Academy of Sciences*, 119(3):e2112566119, 2022.
- [5] Eivinas Butkus, Zhuofan Ying, and Nikolaus Kriegeskorte. How attention saves energy in vision. *bioRxiv*, 2026. doi: 10.64898/2026.03.18.710397.
- [6] Beth L. Chen, David H. Hall, and Dmitri B. Chklovskii. Wiring optimization can relate neuronal structure and function. *Proceedings of the National Academy of Sciences of the United States of America*, 103(12):4723–4728, March 2006. ISSN 0027-8424. doi: 10.1073/pnas.0506806103.
- [7] Ricky T. Q. Chen, Yulia Rubanova, Jesse Bettencourt, and David Duvenaud. Neural Ordinary Differential Equations, December 2019. URL <http://arxiv.org/abs/1806.07366>. arXiv:1806.07366 [cs].
- [8] Dmitri B Chklovskii, Thomas Schikorski, and Charles F Stevens. Wiring optimization in cortical circuits. *Neuron*, 34(3):341–347, 2002.
- [9] Jia Deng, Wei Dong, Richard Socher, Li-Jia Li, Kai Li, and Li Fei-Fei. Imagenet: A large-scale hierarchical image database. In *2009 IEEE Conference on Computer Vision and Pattern Recognition*, pages 248–255, 2009. doi: 10.1109/CVPR.2009.5206848.
- [10] A. Aldo Faisal, Luc P. J. Selen, and Daniel M. Wolpert. Noise in the nervous system. *Nature Reviews Neuroscience*, 9(4):292–303, April 2008. ISSN 1471-003X, 1471-0048. doi: 10.1038/nrn2258. URL <https://www.nature.com/articles/nrn2258>.
- [11] Jonathan Frankle and Michael Carbin. The lottery ticket hypothesis: Finding sparse, trainable neural networks. In *International Conference on Learning Representations*, 2019. URL <https://openreview.net/forum?id=rJ1-b3RcF7>.
- [12] Robert Geirhos, Kristof Meding, and Felix A. Wichmann. Beyond accuracy: quantifying trial-by-trial behaviour of CNNs and humans by measuring error consistency. *Advances in Neural Information Processing Systems*, 33:13890–13902, 2020. URL https://proceedings.neurips.cc/paper_files/paper/2020/hash/9f6992966d4c363ea0162a056cb45fe5-Abstract.html.
- [13] Samuel J Gershman, Eric J Horvitz, and Joshua B Tenenbaum. Computational rationality: A converging paradigm for intelligence in brains, minds, and machines. *Science*, 349(6245):273–278, 2015.
- [14] Alex Graves. Adaptive computation time for recurrent neural networks. *arXiv preprint arXiv:1603.08983*, 2016.
- [15] Song Han, Jeff Pool, John Tran, and William Dally. Learning both weights and connections for efficient neural network. In C. Cortes, N. Lawrence, D. Lee, M. Sugiyama, and R. Garnett, editors, *Advances in Neural Information Processing Systems*, volume 28. Curran Associates, Inc., 2015. URL https://proceedings.neurips.cc/paper_files/paper/2015/file/ae0eb3eed39d2bcef4622b2499a05fe6-Paper.pdf.
- [16] Song Han, Huizi Mao, and William J. Dally. Deep Compression: Compressing Deep Neural Networks with Pruning, Trained Quantization and Huffman Coding, February 2016. URL <http://arxiv.org/abs/1510.00149>. arXiv:1510.00149 [cs].
- [17] Geoffrey Hinton, Oriol Vinyals, and Jeff Dean. Distilling the knowledge in a neural network. *arXiv preprint arXiv:1503.02531*, 2015.

- [18] Mark K. Ho, David Abel, Carlos G. Correa, Michael L. Littman, Jonathan D. Cohen, and Thomas L. Griffiths. People construct simplified mental representations to plan. *Nature*, 606(7912):129–136, June 2022. ISSN 0028-0836, 1476-4687. doi: 10.1038/s41586-022-04743-9. URL <https://www.nature.com/articles/s41586-022-04743-9>.
- [19] Tim C. Kietzmann, Courtney J. Spoerer, Lynn K. A. Sørensen, Radoslaw M. Cichy, Olaf Hauk, and Nikolaus Kriegeskorte. Recurrence is required to capture the representational dynamics of the human visual system. *Proceedings of the National Academy of Sciences*, 116(43):21854–21863, October 2019. ISSN 0027-8424, 1091-6490. doi: 10.1073/pnas.1905544116. URL <https://pnas.org/doi/full/10.1073/pnas.1905544116>.
- [20] Alex Krizhevsky. Learning multiple layers of features from tiny images. Technical report, University of Toronto, Toronto, Ontario, 2009.
- [21] Simon B Laughlin and Terrence J Sejnowski. Communication in neuronal networks. *Science*, 301(5641):1870–1874, 2003.
- [22] Gilles Laurent. On the value of model diversity in neuroscience. *Nature Reviews Neuroscience*, 21(8):395–396, 2020.
- [23] Ya Le and Xuan Yang. Tiny imagenet visual recognition challenge. *CS 231N*, 7(7):3, 2015.
- [24] Yann LeCun, John Denker, and Sara Solla. Optimal brain damage. *Advances in neural information processing systems*, 2, 1989.
- [25] Yann LeCun, Léon Bottou, Yoshua Bengio, and Patrick Haffner. Gradient-based learning applied to document recognition. *Proceedings of the IEEE*, 86(11):2278–2324, 1998.
- [26] Hao Li, Asim Kadav, Igor Durdanovic, Hanan Samet, and Hans Peter Graf. Pruning Filters for Efficient ConvNets, March 2017. URL <http://arxiv.org/abs/1608.08710>. arXiv:1608.08710 [cs].
- [27] Falk Lieder and Thomas L Griffiths. Resource-rational analysis: Understanding human cognition as the optimal use of limited computational resources. *Behavioral and Brain Sciences*, 43:e1, 2020.
- [28] Jack Lindsey, Samuel A Ocko, Surya Ganguli, and Stephane Deny. A unified theory of early visual representations from retina to cortex through anatomically constrained deep cnns. *arXiv preprint arXiv:1901.00945*, 2019.
- [29] Chenxi Liu, Barret Zoph, Maxim Neumann, Jonathon Shlens, Wei Hua, Li-Jia Li, Li Fei-Fei, Alan Yuille, Jonathan Huang, and Kevin Murphy. Progressive neural architecture search. In *Proceedings of the European conference on computer vision (ECCV)*, pages 19–34, 2018.
- [30] Hanxiao Liu, Karen Simonyan, and Yiming Yang. DARTS: Differentiable architecture search. In *International Conference on Learning Representations*, 2019. URL <https://openreview.net/forum?id=S1eYHoC5FX>.
- [31] Zhuang Liu, Jianguo Li, Zhiqiang Shen, Gao Huang, Shoumeng Yan, and Changshui Zhang. Learning efficient convolutional networks through network slimming. In *Proceedings of the IEEE international conference on computer vision*, pages 2736–2744, 2017.
- [32] Eshed Margalit, Hyodong Lee, Dawn Finzi, James J. DiCarlo, Kalanit Grill-Spector, and Daniel L.K. Yamins. A unifying framework for functional organization in early and higher ventral visual cortex. *Neuron*, 112(14):2435–2451.e7, July 2024. ISSN 08966273. doi: 10.1016/j.neuron.2024.04.018. URL <https://linkinghub.elsevier.com/retrieve/pii/S0896627324002794>.
- [33] Joshua C Peterson, Ruairidh M Battleday, Thomas L Griffiths, and Olga Russakovsky. Human uncertainty makes classification more robust. In *Proceedings of the IEEE/CVF international conference on computer vision*, pages 9617–9626, 2019.
- [34] Herbert A Simon. A behavioral model of rational choice. *The quarterly journal of economics*, pages 99–118, 1955.
- [35] Charlie Snell, Jaehoon Lee, Kelvin Xu, and Aviral Kumar. Scaling llm test-time compute optimally can be more effective than scaling model parameters. *arXiv preprint arXiv:2408.03314*, 2024.
- [36] Courtney J. Spoerer, Patrick McClure, and Nikolaus Kriegeskorte. Recurrent Convolutional Neural Networks: A Better Model of Biological Object Recognition. *Frontiers in Psychology*, 8:1551, September 2017. ISSN 1664-1078. doi: 10.3389/fpsyg.2017.01551. URL <https://www.frontiersin.org/article/10.3389/fpsyg.2017.01551/full>.

- [37] Courtney J Spoerer, Tim C Kietzmann, Johannes Mehrer, Ian Charest, and Nikolaus Kriegeskorte. Recurrent neural networks can explain flexible trading of speed and accuracy in biological vision. *PLOS Computational Biology*, 16(10):e1008215, 2020.
- [38] Peter Sterling and Simon Laughlin. *Principles of neural design*. MIT Press, 2015.
- [39] Simon Thorpe, Denis Fize, and Catherine Marlot. Speed of processing in the human visual system. *Nature*, 381(6582):520–522, 1996.
- [40] Edward Vul, Noah Goodman, Thomas L Griffiths, and Joshua B Tenenbaum. One and done? Optimal decisions from very few samples. *Cognitive science*, 38(4):599–637, 2014.
- [41] Matthew D Zeiler and Rob Fergus. Visualizing and understanding convolutional networks. In *European conference on computer vision*, pages 818–833. Springer, 2014.

A Compute

Each model was trained on a single GPU for approximately 2.5 hours, requiring roughly 3.3 GB of GPU memory at batch size 128. Training was conducted on a university cluster with a mix of NVIDIA GeForce RTX 2080 Ti, A40, and L40 GPUs. The 1,273 models reported in this paper required approximately 3,200 GPU-hours in total. Additional compute was used during model development and preliminary experiments but was not formally tracked.

B Experiments

Table 1: Summary of experimental configurations. Total models is the product of all variable levels and the number of instances. The breadth vs. depth results use the $\lambda_{\text{time}} = 0$ slice of the three-way experiment.

Experiment	Variable	Values	Instances	Models
Breadth vs. depth vs. time	λ_{breadth}	{0, 1, 10, 10 ² , 10 ³ , 10 ⁴ }	3	648
	λ_{depth}	{0, 1, 10, 10 ² , 10 ³ , 10 ⁴ }		
	λ_{time}	{0, 0.1, 0.2, 0.3, 0.5, 1.0}		
Time	scheme	{fixed, adaptive}	10	220
	λ_{time}	{0, 0.1, 0.2, ..., 1.0}		
Task complexity	dataset	{MNIST, CIFAR-10, Tiny ImageNet}	5	405
	λ_{breadth}	{1, 10, 10 ² }		
	λ_{depth}	{1, 10, 10 ² }		
	λ_{time}	{0.1, 0.2, 0.5}		
Total				1273

C Noise

An artificial neural network without internal noise could arbitrarily scale down all its weights to minimize the breadth and depth costs without affecting performance. Biological neural systems, by contrast, contend with multiple sources of noise that corrupt neural signals [10]. We add Gaussian noise ($\sigma = 0.1$) to the hidden states at each time step, establishing a floor below which weights cannot be reduced without degrading signal-to-noise ratio. The specific value of σ is arbitrary in the sense that it sets the scale against which weight magnitudes are measured. The network adjusts its weights relative to this noise floor. We chose $\sigma = 0.1$ as it is large enough to prevent trivial weight scaling while remaining small enough not to disrupt learning when annealed. Noise makes the magnitude-based resource costs meaningful: the network must maintain sufficiently large weights to overcome the noise, so reducing a channel’s weights under resource pressure has a real cost in performance. Noise is annealed during training to ensure stable early learning.

D Annealing Noise and Resource Costs

During an initial warmup period, resource costs are set to zero, allowing the network to first learn useful representations under the error cost alone. Resource costs are then linearly annealed to their full values over a fixed number of epochs (warmup: 15 epochs for space costs, 20 for time; annealing: 10 epochs for both). Noise is similarly annealed, starting from zero and linearly increasing to its full magnitude ($\sigma = 0.1$) over the first 15 epochs. This staged schedule prevents the resource costs from interfering with early learning, and ensures the noise floor is established before the costs are fully active.

E Training Details

All models are trained for 150 epochs using AdamW ($\text{lr} = 10^{-3}$, $\beta = (0.9, 0.999)$, weight decay = 0.1) with mixed-precision training. The learning rate follows a warmup-hold-cosine schedule: linear warmup for 5 epochs, held constant for 25 epochs (so costs are fully active before decay begins), then cosine decay to 10^{-6} over the remaining 120 epochs. Gradients are clipped to a maximum norm of 1.0.

F Pruning Algorithm

We use an iterative binary search procedure to determine the effective number of layers and channels used by each trained model. The goal is to find the smallest sub-network that preserves 98% of the model’s above-chance accuracy.

We define the accuracy threshold as:

$$\text{acc}_{\text{threshold}} = \text{acc}_{\text{chance}} + 0.98 \cdot (\text{acc}_{\text{baseline}} - \text{acc}_{\text{chance}}) \tag{6}$$

where $\text{acc}_{\text{baseline}}$ is the unpruned model’s test accuracy and $\text{acc}_{\text{chance}} = 1/K$ for K classes.

Each channel in each layer is assigned a norm equal to its average weight magnitude across all convolutional kernels (the same ranking used by the breadth cost during training). We then perform a binary search in log-space over a norm threshold: all channels with norm below the threshold are zeroed out. At each iteration, we evaluate accuracy on 10,000 test images. If accuracy falls below the threshold, we lower the norm cutoff (preserving more channels). Otherwise, we raise it (pruning more aggressively). We run 30 iterations of binary search, which is sufficient for convergence.

The final pruning mask is a binary matrix of shape (layers \times channels). From this mask, we define *layers used* (depth) as the number of layers with at least one surviving channel, and *channels used* (breadth) as the average number of surviving channels per active layer.

G Attribution

We used an image perturbation method to estimate which spatial regions are important for classification. Gaussian noise ($\sigma = 0.05$) was added to raw pixel values within a 5×5 sliding window (stride 1), producing a set of perturbed images, each with one noisy patch at a unique location. The attribution score for a given patch was computed as the drop in the model’s predicted probability for the correct class: $s_{\text{patch}} = p_c^{\text{orig}} - p_c^{\text{pert}}$, where p_c^{orig} and p_c^{pert} are the softmax probabilities for the correct class c on the original and perturbed images, respectively. Each pixel’s final score was computed as the average s_{patch} across all patches containing that pixel.

H Supplemental Figures

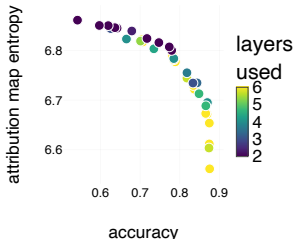


Figure 7: Attribution map entropy as a function of accuracy and number of layers used. At matched accuracy levels, there is a trend toward higher entropy for shallower models, but the effect is small. A more controlled investigation is left for future work.